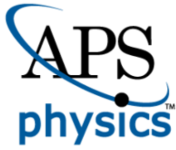

CHORUS

This is the accepted manuscript made available via CHORUS. The article has been published as:

Identifying different stacking sequences in few-layer CVD-grown MoS_{2} by low-energy atomic-resolution scanning transmission electron microscopy

Aiming Yan, Wei Chen, Colin Ophus, Jim Ciston, Yuyuan Lin, Kristin Persson, and Alex Zettl

Phys. Rev. B **93**, 041420 — Published 25 January 2016

DOI: 10.1103/PhysRevB.93.041420

Identifying different stacking sequences in few-layer CVD-grown MoS_2 by low-energy atomic-resolution STEM

Aiming Yan[±,§,#], *Wei Chen*[⊥,†], *Colin Ophus*[‖], *Jim Ciston*[‖], *Yuyuan Lin*[‡], *Kristin Persson*[⊥], *Alex Zettl*[±,§,#,*1]

[±]Department of Physics, University of California, Berkeley, CA 94720, USA

[⊥]Electrochemical Technologies Group, Lawrence Berkeley National Laboratory, Berkeley CA 94720, USA

[‖]National Center for Electron Microscopy, Molecular Foundry, Lawrence Berkeley National Laboratory, Berkeley CA 94720, USA

[†]Department of Mechanical, Materials & Aerospace Engineering, Illinois Institute of Technology, Chicago, IL 60616, USA

[‡]Department of Materials Science and Engineering, Northwestern University, Evanston, IL 60208, USA

[1] * Corresponding author: azettl@berkeley.edu

[§]Materials Sciences Division, Lawrence Berkeley National Laboratory, Berkeley, CA 94720, USA

[#]Kavli Energy NanoSciences Institute at the University of California, Berkeley and the Lawrence Berkeley National Laboratory, Berkeley, CA 94720, USA

ABSTRACT:

Atomically thin MoS_2 grown by chemical vapor deposition (CVD) is a promising candidate for the next-generation electronics due to inherent CVD scalability and controllability. However, it is well-known that the stacking sequence in few-layer MoS_2 can significantly impact the electrical and optical properties. Herein we report different intrinsic stacking sequences in CVD grown few-layer MoS_2 obtained by atomic-resolution annular-dark-field imaging in an aberration-corrected scanning transmission electron microscope operated at 50 keV. Tri-layer MoS_2 displays a new stacking sequence distinct from the commonly observed 2H and 3R phases of MoS_2. Density functional theory is used to examine the stability of different stacking sequences, and the findings are consistent with our experimental observations.

I. INTRODUCTION

Atomically thin molybdenum disulfide (MoS_2) has recently attracted significant attention due to its novel physical and electrical properties. Single-layer MoS_2 (extracted from naturally occurring 2-H-phase material) has a direct electronic band gap ~1.8 eV [1,2] while bulk 2-H phase MoS_2 exhibits a lower indirect band gap ~ 1.3eV [3]. This semiconducting nature has been exploited to create MoS_2 field effect transistors (FETs) [4] with high on-off ratio and

ultrasensitive photodetectors [5], amongst other optoelectronic and photonic [6,7] devices. The number of layers not only provides tunability of the band gap of MoS_2 for photonic applications [8], but also performance enhancements that may not be directly gap related. For instance, the gas sensing behavior of few-layer thick MoS_2 has been found to be better than that of single-layer MoS_2 due to the instability of the single-layer form in reactive gas environments [9,10]. Another example is that few-layer MoS_2 usually displays higher carrier mobility than that of single-layer MoS_2 in various heterostructured FET configurations [11–13].

The stacking sequence is a major structural factor that controls the properties of few-layer MoS_2. Theoretical calculations have predicted that the stacking sequence in bi-layer MoS_2 plays an important role in its electronic band structure [14]. Experimental studies have found that the relative rotation angle in bi-layer MoS_2 significantly modifies the direct/indirect band gap and interlayer coupling [15,16]. The recently observed spin/valley polarization in symmetry-breaking 3R phase bulk MoS_2 (another commonly observed phase of bulk MoS_2) further elucidates the key role of stacking sequences (or crystal structure) in the properties of layered MoS_2 [17].

Single- and few-layer MoS_2 grown by chemical vapor deposition (CVD) methods has great potential in building next-generation electronics due to the inherent controllability and scalability [18,19] of CVD growth. A thorough understanding of the structure of CVD grown MoS_2 is essential for full exploration of its applications. Here we demonstrate a precise determination of different stacking sequences in CVD grown few-layer MoS_2 by employing atomic-resolution annular-dark-field (ADF) imaging in scanning transmission electron microscopy (STEM) using an unusually low electron beam energy (50 keV). Notably, this energy is much lower than the 80 keV threshold for knock-on damage to MoS_2 [20]; this allows for extended study of pristine multi-layer MoS_2 at the atomic scale. We find that the stacking

sequence in CVD grown MoS_2 is layer-dependent, and can be a mixture of 2H and 3R phases of MoS_2 in tri-layer form. Density functional theory (DFT) calculations confirm that the stacking sequences observed in our CVD grown few-layer MoS_2 are among the most stable configurations.

II. EXPERIMENTAL AND THEORETICAL DETAILS:

We use a two-zone furnace to grow single-layer and few-layer (bi-layer and tri-layer) MoS_2 on SiO_2/Si substrates as described previously [21]. A quartz tube contains S and MoO_3 precursors, with S in zone 1 and MoO_3 precursor in zone 2. SiO_2/Si chips are placed on top of the crucible that contains the MoO_3 precursor. N_2 gas flows through the quartz tube during the whole growth process. Zone 1 and zone 2 are first kept at 105 °C for 3 hours to warm up the precursors and 200 sccm N_2 flows through the tube. The temperature of zone 2 is then slowly increased to 500 °C (over 30 minutes) while zone 1 is kept at 105 °C. These temperatures are maintained for 30 minutes. The temperatures of zones 1 and 2 are then raised to 400 °C and 780 °C (over 30 minutes) respectively, and N_2 flow rate is changed to 9 sccm. The 400 °C and 780 °C temperatures are maintained for 10 minutes, after which the furnace is turned off and cooled to room temperature naturally.

We use optical microscopy and Raman spectroscopy to initially characterize single-layer and few-layer MoS_2 grown on SiO_2/Si by CVD method (see examples shown in Supplemental Material Sec. 1 [22]) before transferring the flakes onto quantifoil® TEM grids. Previous studies have shown that single-layer MoS_2 grown on SiO_2/Si by the CVD method displays a direct band gap and shows a strong photoluminescence (PL) peak centered around 1.84 eV at room temperature [18,19]. Double-layer CVD grown MoS_2 has an indirect band gap and shows a

slightly red-shifted PL peak compared to the single-layer form. These distinctions aid in initial sample layer number identification.

TEM samples for STEM ADF imaging are prepared by a "direct transfer" [23]. A quantifoil® TEM grid is placed on the targeted MoS_2 flakes grown on the SiO_2/Si substrate and a drop of IPA is placed next to the TEM grid. After the IPA evaporates completely, the SiO_2/Si substrate with TEM grid is placed into potassium hydroxide (KOH) solution (~ 10%) overnight. After etching away the SiO_2, the TEM grid with MoS_2 flakes is detached from the Si substrate. The TEM grid is then rinsed in DI water several times. Immediately before imaging, the TEM grid with MoS_2 flakes is annealed in forming gas (Ar:H_2 = 200 sccm:50 sccm) at 250 °C for 3 hours.

Atomic-resolution STEM ADF imaging is performed on TEAM 0.5, a double-aberration-corrected (scanning) transmission electron microscope (STEM/TEM) located in the National Center for Electron Microscopy (NCEM) at the Molecular Foundry, Lawrence Berkeley National Laboratory. The microscope is here operated at 50 keV to minimize radiation damage to the sample. For STEM ADF imaging, a probe size of ~1.7 Å, a convergence angle of 32 mrad and collection angles of 77 mrad to 385 mrad are used.

Total energy calculations are carried out using density functional theory (DFT) and the projector augmented-wave (PAW) approach as implemented in the Vienna ab initio simulation package(VASP) [14,24,25]. The generalized gradient approximation (GGA) of Perdew-Burke-Ernzerhof (PBE) is used to approximate the electronic exchange and correlation. The interlayer van der Waals interactions are considered using a correction scheme by Grimme [24]. We model

MoS_2 stacking using a slab model with a vacuum layer of at least 20 Angstrom. All structures are relaxed until the energy has converged within 10^{-6} eV/unit cell.

III. RESULTS AND DISCUSSION

As a member of transition mental dichalcogenides (TMDs) having rich polytypism [27], bulk MoS_2 presents two commonly observed phases: (1) the 2H phase (space group $P6_3/mmc$) which exists naturally and can also be synthesized via chemical vapor transport (CVT) methods; (2) the 3R phase (space group R3m) which is typically synthesized (again via CVT methods) [17]. The stacking orders for both 2H and 3R phases, in the single-layer, bi-layer and tri-layer configurations, are shown in Figure 1. The nomenclature for the stacking sequence used here is following Refs. [14,28]. Single-layer MoS_2 for both phases has the same structure with one layer of Mo atoms sandwiched between two layers of S atoms. Each layer of Mo and S atoms is arranged in a hexagonal lattice and two S layers have the same in-plane lattice points. For bi-layer MoS_2, the 2H and 3R phases show different stacking sequences for the S-Mo-S sandwiched structure. As shown in Figure 1, 2H phase MoS_2 in the form of bi-layer has a stacking sequence recorded as AA', with Mo eclipsed over S, and the two layers have inversion symmetry. 3R phase MoS_2 in the form of bi-layer has stacking sequence AB, with staggered Mo over S and the two layers do not have inversion symmetry. To determine the stacking sequence for tri-layer MoS_2 of different phases, we treat the second layer as the first layer (as if it were A) and name the stacking sequence for the third layer following the two-layer naming system. Therefore, 2H phase tri-layer MoS_2 has the stacking sequence (AA')A' and 3R phase tri-layer MoS_2 has sequence (AB)B.

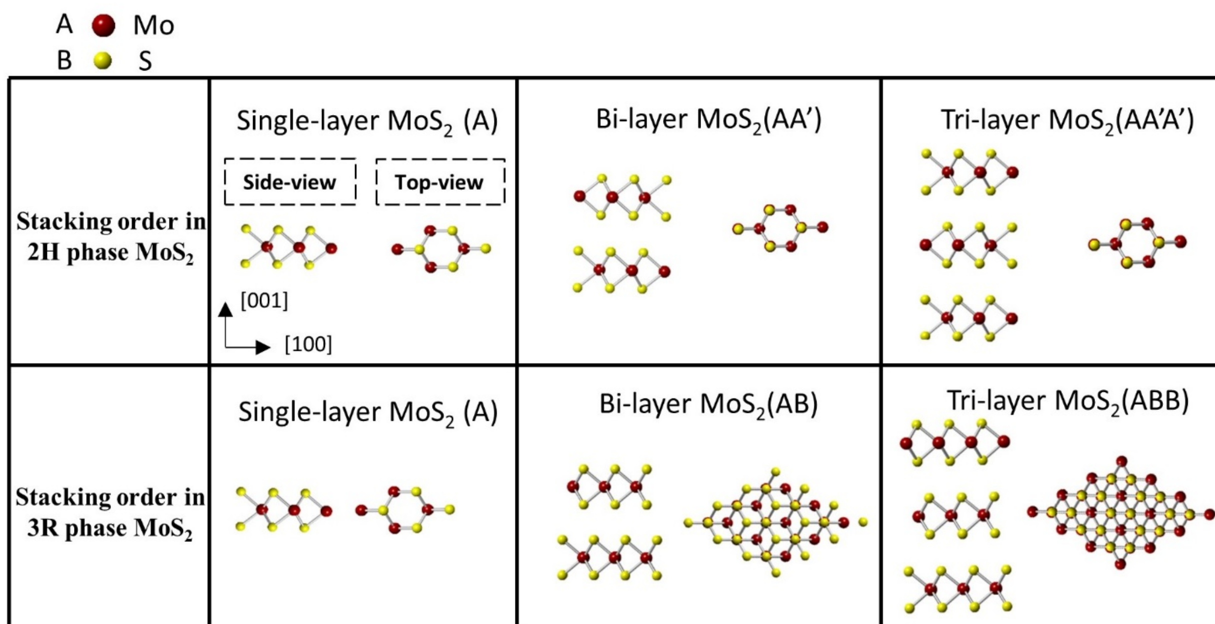

Figure 1: *(Color online) Schematics showing the stacking orders for 2H and 3R phases* MoS_2 *in the form of single layer, bi-layer and tri-layer viewed from side and top. Red spheres represent Mo atoms and yellow spheres represent S atoms.*

ADF STEM imaging is a powerful tool to distinguish different atoms provided that the sample has uniform thickness [29]. Given that: (1) MoS_2 is composed of two atomic species (Mo and S) which have significantly different atomic numbers (Mo- 42, S- 16); and (2) multi-layer MoS_2 is a layered structure with uniform sample thickness for a certain number of layers, ADF imaging serves ideally to identify the type and location of each atom in thin samples. Figure 2 shows the low-magnification ADF image of single-layer, bi-layer and tri-layer MoS_2 suspended over holes of the TEM grid. The layer number can be identified according to the linearly changed intensity in the image after background subtraction (using vacuum as reference) as shown in Figure 2(b).

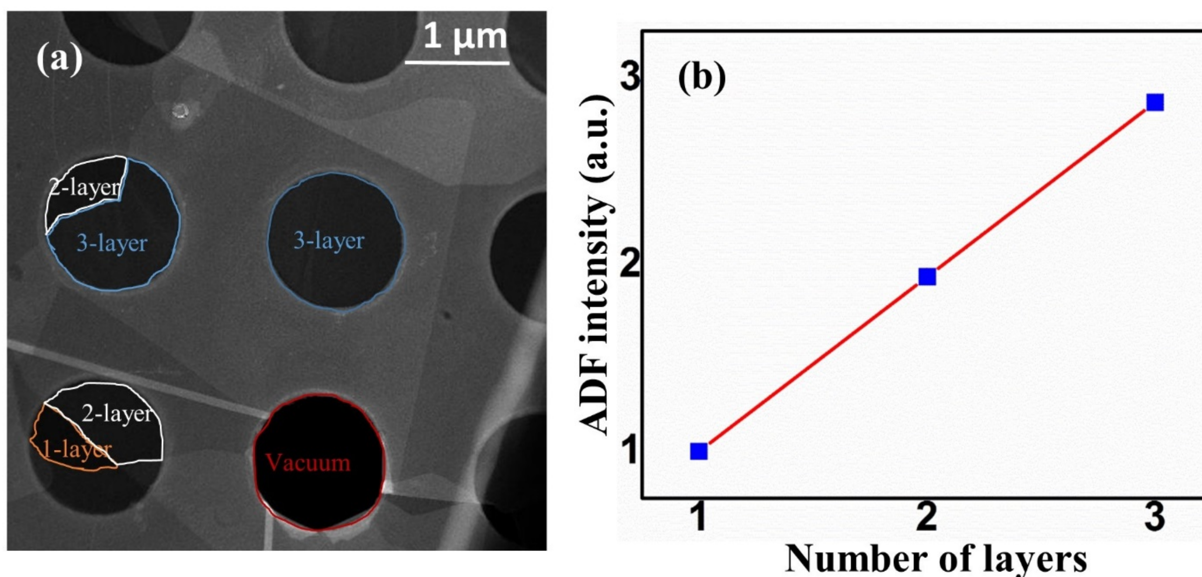

Figure 2: *(Color online) Low-mag ADF image of single-layer, bi-layer and tri-layer MoS_2. (a) Low-mag ADF image of the area where 1-layer, 2-layer and 3-layer CVD grown MoS_2 hang over holes on a quantifoil® TEM grid. The region of vacuum gives the background counts for the whole image. (b) The intensity in the ADF image is linear as a function of the number of layers after background subtraction using vacuum as reference.*

With comparison to simulated ADF images of MoS_2 with known stacking sequences, we identify the stacking sequence in experimental ADF images of CVD grown few-layer MoS_2. In order to improve signal-to-noise ratio in the experimentally obtained ADF images, a few or tens of unit cells from a larger sample area are averaged [30] and presented in Figure 3 (a) (b) and (c), corresponding to single-layer, bi-layer and tri-layer MoS_2 respectively (the same region as shown in Figure 2 (a)). The original ADF images from larger areas of different layer numbers can be found in the Supplemental Material Sec. 2 [22]. Figure 3 (d) (e) and (f) are simulated ADF images based on multi-slice theory [30]. These simulated images provide information regarding symmetry and relative intensity at different atomic sites for a certain stacking sequence. A match

in terms of both symmetry and intensity between simulated and experimental ADF images is essential for the determination of the correct stacking sequence. Experimental ADF images are less sharp than the simulated ones due to incoherence and broadening effect in the real-life electron probe, as well as drifting effects and sample vibration during the imaging process. In the experimental ADF images one often finds overlapping of intensity between neighboring atoms, which blurs the atomic edges. The experimental ADF image of single-layer MoS_2 (Figure 3(a)) shows distinct intensity at two sublattices for Mo and S respectively, with red spheres representing Mo and overlapping yellow spheres representing S. A simulated ADF image of single-layer MoS_2 (Figure 3(d)) shows the same symmetry as the experimental ADF image. The line scans across Mo and S sublattice points in experimental and simulated images (Figure 3(g)) show the same ratio of relative intensity. With the same analysis method, we find that a great portion (> 50%) of bi-layer CVD grown MoS_2 takes the stacking sequence of AA'. An experimental ADF image of such a stacking sequence is shown in Figure 3(b), in which we consistently observe intensity differences around 15% at two sublattices with 3-fold symmetry. This is in accord with the multi-slice simulation shown in Figure 3(e). The line scans across the inequivalent two lattice points in experimental and simulated ADF images are compared in Figure 3(h), which show a good match in relative intensity. Non-zero relative rotation angles between the two layers are also observed in our bi-layer MoS_2 samples, which is common in CVD grown MoS_2 (see Supplemental Material Sec. 3 [22] and ref. [18]).

A new symmetry-breaking stacking sequence is found in our CVD grown tri-layer MoS_2. This stacking sequence is identified to be (AA')B after we compare the experimental and simulated ADF images of tri-layer MoS_2 with stacking sequences that have AA' stacking for the first two layers (see Supplemental Material Sec. 4). In AA'B stacked tri-layer MoS_2, the third

layer is staggered, with S atoms over Mo atoms of the second layer as shown schematically in Figure 4 (a). There are three distinct lattice points in AA'B stacked tri-layer MoS_2 as shown in the experimental (Figure 3(c)) and simulated (Figure 3(f)) ADF images. The line scans across these three lattice points (Figure 3(i)) in experimental and simulated ADF images show that the ratio of intensity for these three lattice points is 1:0.55:0.45 and 1:0.65:0.5 respectively, in reasonable agreement. CVD grown tri-layer MoS_2 with stacking sequence AA'B is consistently observed (> 50%) across the same sample and in samples from different growth batches (see Supplemental Material Sec. 5 [22]).

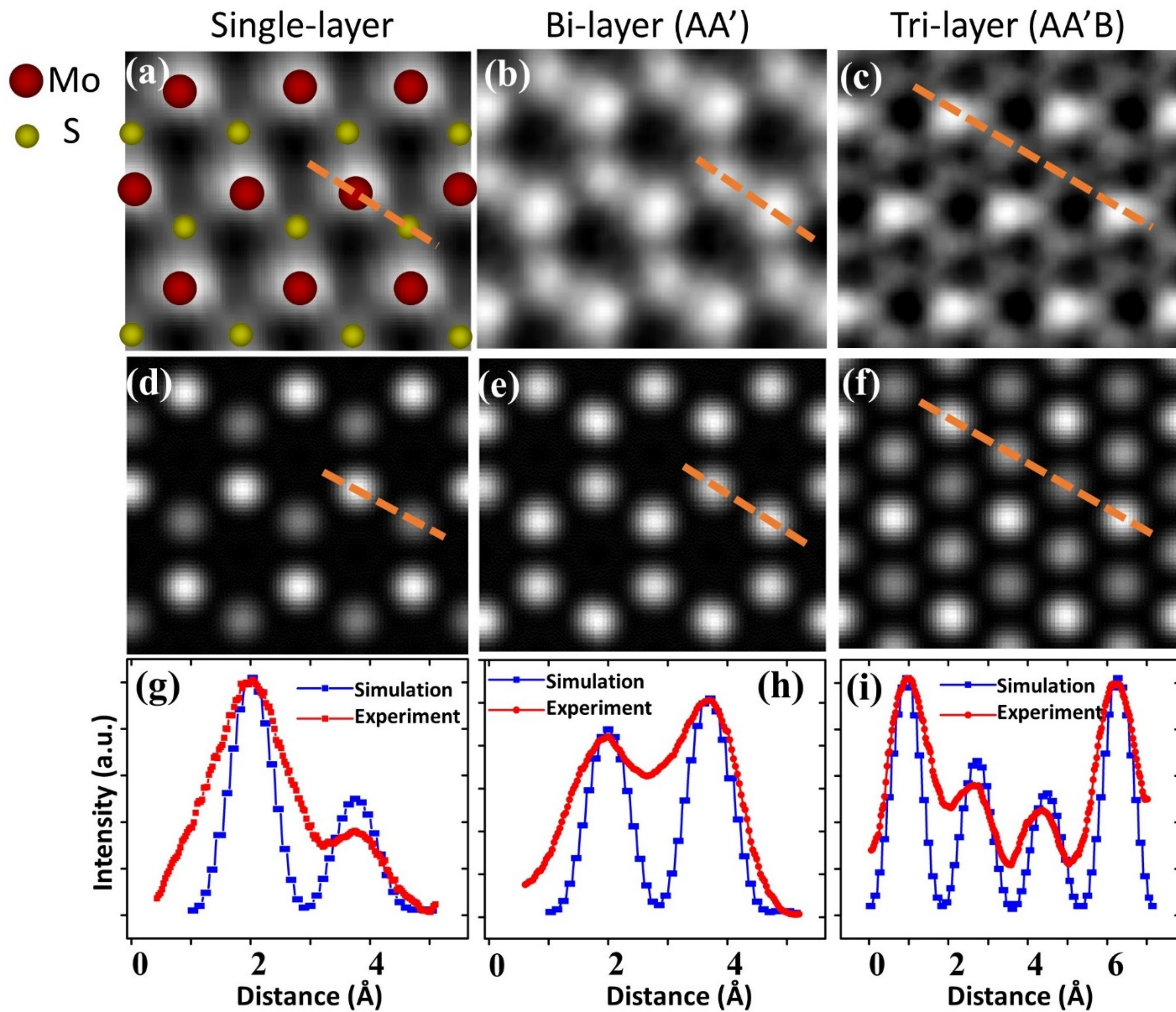

Figure 3: *(Color online) Atomic-resolution ADF images of single-layer, bi-layer (AA' stacking) and tri-layer (AA'B stacking) CVD grown* MoS_2 *in comparison with simulated images. (a) (b) and (c), the experimentally observed atomic-resolution ADF images of single-layer, bi-layer (AA' stacking) and tri-layer (AA'B stacking) CVD grown* MoS_2 *respectively, after averaging the intensity of more than 10 unit cells from a larger area of the same stacking sequence. (d) (e) and (f), multi-slice simulation of ADF images of single-layer, bi-layer (AA' stacking) and tri-layer (AA'B stacking)* MoS_2 *with the same beam energy, convergence angle and collection angles for the experiment. (g) (h) and (i), line scans across lattice points indicated by the orange lines in (a)(b)(c) and (d)(e)(f), showing the comparison of intensity of these lattice points in simulated and experimental ADF images for single-layer, bi-layer (AA' stacking) and tri-layer (AA'B stacking) CVD grown* MoS_2 *respectively.*

To understand the prevalence of AA'B stacking sequence over other stacking possibilities in the tri-layer MoS_2, we perform first-principles calculations to study the preference of different stacking sequences of MoS_2. All possible bi-layer (five) and tri-layer (fifteen) stacking sequences of MoS_2 are calculated and the total energies are compared in Figs. 4(b) and (c) respectively (absolute values for all stacking possibilities are in Supplemental Material Sec. 6 [22]). Here, the calculated energy is the total energy from solving the Kohn-Sham equation [31] plus the dispersion corrections by Grimme [26]. For bi-layer MoS_2, as expected the stacking sequences with the lowest energies are AA' and AB, which corresponds to bi-layer form of 2H and 3R phase respectively (outlined by orange circles in Fig. 4 (b)). Our calculation results of bi-layer MoS_2 are comparable to those of ref [14]. These two stacking sequences are close in energy and are commonly observed in experimental studies. In our CVD grown bi-layer MoS_2, AA' stacking is prevalent over AB stacking. Similarly, there are three tri-layer stacking

possibilities with nearly degenerate calculated energy as outlined by orange circles in Fig. 4 (c): (AA')A', (AA')B and (AB)B (the energy differences are within typical DFT error, so a true ground state is not determined). Importantly, the experimentally observed (AA')B stacking in CVD grown tri-layer MoS_2 is among these predicted minimum energy configurations. Moreover, the (AA')B stacking sequence is dominant in our CVD grown tri-layer MoS_2, and indicates that our growth conditions favor this stacking over other low-energy stacking sequences, probably due to the higher energy barriers required by those stacking configurations.

CVD grown few-layer MoS_2 with different stacking sequences reported here is relevant to the electronic and optical properties of this material. Specifically, distinct layer-dependent valley polarization phenomena in few-layer 2H and 3R phases of MoS_2 [17] suggest that tri-layer CVD grown MoS_2 with mixed stacking sequences (AA'B) may present a new valley polarization signature different from those of both phases of tri-layer form. In addition, we speculate the layer-dependent stacking sequence observed in our CVD grown few-layer MoS_2 is likely controlled synergistically by various growth parameters. These parameters include growth temperature, feeding rate and partial pressure of the precursors, which can change slightly over time during the material's nucleation and growth process. Because CVD growth of few-layer MoS_2 follows the so-called "layer-by-layer" growth mechanism [32], the slight change of growth parameters over time will cause the change of preferred stacking sequence for a certain layer number.

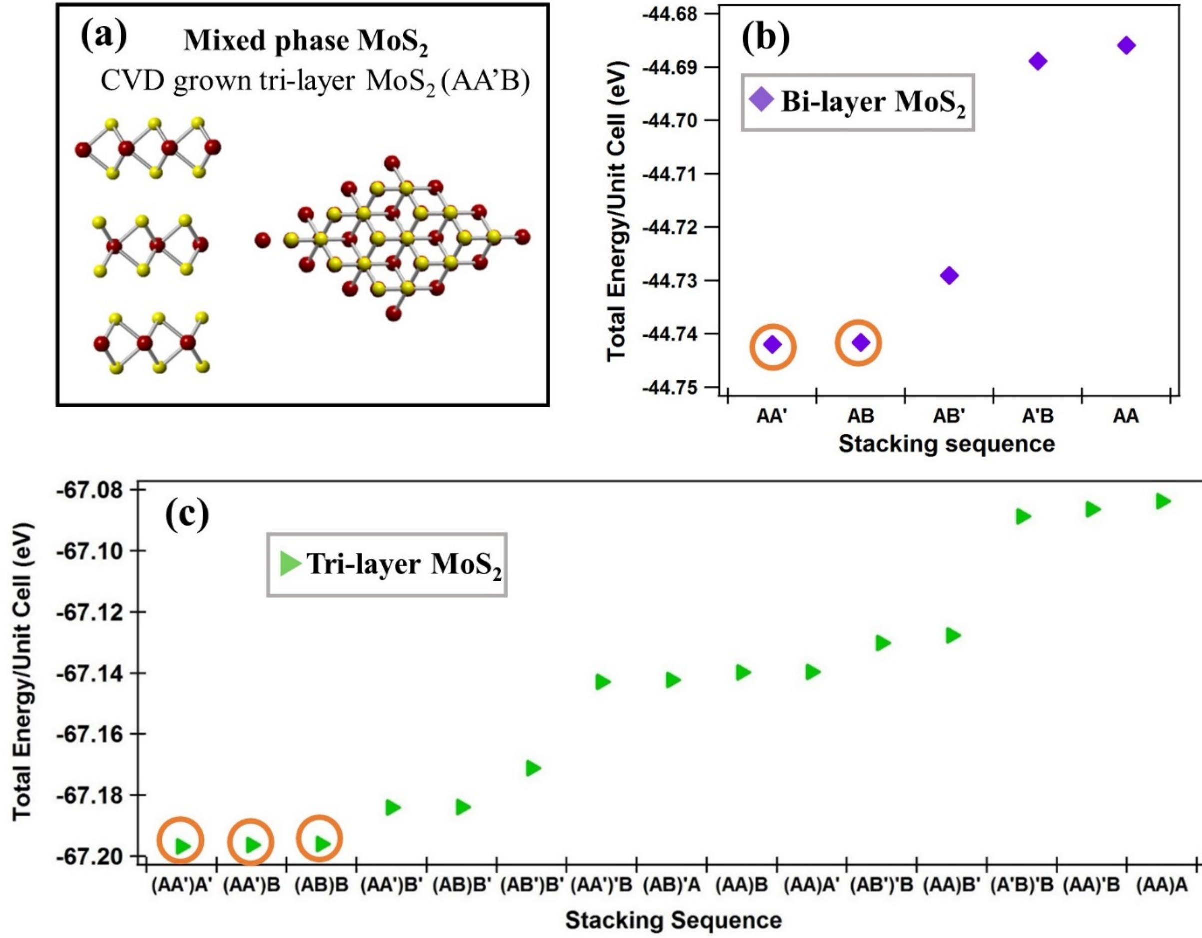

Figure 4: *(Color online) (a) the crystal structure of tri-layer MoS_2 with the stacking sequence AA'B viewed from side (on the left) and top (on the right); (b) total energies of all possible stacking sequences for bi-layer MoS_2, obtained from first-principles calculations; (c) total energies of all possible stable stacking sequences for tri-layer MoS_2, obtained from first-principles calculations.*

IV. SUMMARY AND CONCLUSIONS

Atomic-resolution STEM imaging is successfully employed to precisely determine different stacking sequences in few-layer CVD grown MoS_2. The stacking sequence in bi-layer and tri-layer MoS_2 are found to differ. The 2H phase is consistently observed for bi-layer CVD

grown MoS_2, which has the stacking sequence AA' with inversion symmetry. The stacking sequence AA'B is observed for the majority of CVD grown tri-layer MoS_2, which shows broken inversion symmetry. First-principles calculations show that the AA'B stacking sequence is among the most stable configurations, with the other two stacking possibilities of AA'A' (2H phase) and ABB (3R phase). Due to the symmetry-breaking nature of tri-layer CVD grown MoS_2, this configuration should be of great interest for valley polarization study.

ACKNOWLEDGEMENTS

This research was supported in part by the Director, Office of Basic Energy Sciences, Materials Sciences and Engineering Division, of the U.S. Department of Energy under Contract DE-AC02-05CH11231, within the sp2-bonded Materials Program, which provided for postdoctoral support and AFM and PL characterization; by NSF grant DMR-1206512 which provided for the sample growth; and by the Molecular Foundry of the Lawrence Berkeley National Laboratory, under Contract DE-AC02-05CH11231, which provided for TEM characterization. We acknowledge Chengyu Song in the Molecular Foundry of the Lawrence Berkeley National Laboratory for TEM technical support. The first-principles modeling work was supported by the Materials Project Center under the DOE Basic Energy Sciences Grant No. EDCBEE.

REFERENCES

[1] K. F. Mak, C. Lee, J. Hone, J. Shan, and T. F. Heinz, Phys. Rev. Lett. **105**, (2010).

[2] A. Splendiani, L. Sun, Y. B. Zhang, T. S. Li, J. Kim, C. Y. Chim, G. Galli, and F. Wang,

Nano Lett. **10**, 1271 (2010).

[3] K. K. Kam and B. A. Parkinson, J. Phys. Chem. **86**, 463 (1982).

[4] B. Radisavljevic, A. Radenovic, J. Brivio, V. Giacometti, and A. Kis, Nat. Nanotechnol. **6**, 147 (2011).

[5] O. Lopez-Sanchez, D. Lembke, M. Kayci, A. Radenovic, and A. Kis, Nat. Nanotechnol. **8**, 497 (2013).

[6] Z. Yin, H. Li, H. Li, L. Jiang, Y. Shi, Y. Sun, G. Lu, Q. Zhang, X. Chen, and H. Zhang, ACS Nano **6**, 74 (2011).

[7] M. Buscema, M. Barkelid, V. Zwiller, H. S. J. van der Zant, G. A. Steele, and A. Castellanos-Gomez, Nano Lett. **13**, 358 (2013).

[8] H. S. Lee, S. W. Min, Y. G. Chang, M. K. Park, T. Nam, H. Kim, J. H. Kim, S. Ryu, and S. Im, Nano Lett. **12**, 3695 (2012).

[9] H. Li, Z. Y. Yin, Q. Y. He, X. Huang, G. Lu, D. W. H. Fam, A. I. Y. Tok, Q. Zhang, and H. Zhang, Small **8**, 63 (2012).

[10] D. J. Late, Y. K. Huang, B. Liu, J. Acharya, S. N. Shirodkar, J. Luo, A. Yan, D. Charles, U. V. Waghmare, V. P. Dravid, and C. N. R. Rao, ACS Nano **7**, 4879 (2013).

[11] W. Bao, X. Cai, D. Kim, K. Sridhara, and M. S. Fuhrer, Appl. Phys. Lett. **102**, 42104 (2013).

[12] G.-H. Lee, Y.-J. Yu, X. Cui, N. Petrone, C.-H. Lee, M. S. Choi, D.-Y. Lee, C. Lee, W. J. Yoo, K. Watanabe, T. Taniguchi, C. Nuckolls, P. Kim, and J. Hone, ACS Nano **7**, 7931 (2013).

[13] M. S. Choi, G.-H. Lee, Y.-J. Yu, D.-Y. Lee, S. H. Lee, P. Kim, J. Hone, and W. J. Yoo, Nat. Commun. **4**, 1624 (2013).

[14] J. He, K. Hummer, and C. Franchini, Phys. Rev. B **89**, 75409 (2014).

[15] K. Liu, L. Zhang, T. Cao, C. Jin, D. Qiu, Q. Zhou, A. Zettl, P. Yang, S. G. Louie, and F. Wang, Nat. Commun. **5**, (2014).

[16] A. M. van der Zande, J. Kunstmann, A. Chernikov, D. A. Chenet, Y. You, X. Zhang, P. Y. Huang, T. C. Berkelbach, L. Wang, F. Zhang, and others, Nano Lett. **14**, 3869 (2014).

[17] R. Suzuki, M. Sakano, Y. J. Zhang, R. Akashi, D. Morikawa, A. Harasawa, K. Yaji, K. Kuroda, K. Miyamoto, T. Okuda, and others, Nat. Nanotechnol. **9**, 611 (2014).

[18] S. Najmaei, Z. Liu, W. Zhou, X. Zou, G. Shi, S. Lei, B. I. Yakobson, J.-C. Idrobo, P. M. Ajayan, and J. Lou, Nat. Mater. **12**, 754 (2013).

[19] A. M. van der Zande, P. Y. Huang, D. A. Chenet, T. C. Berkelbach, Y. You, G.-H. Lee, T. F. Heinz, D. R. Reichman, D. A. Muller, and J. C. Hone, Nat. Mater. **12**, 554 (2013).

[20] H. P. Komsa, J. Kotakoski, S. Kurasch, O. Lehtinen, U. Kaiser, and A. V Krasheninnikov, Phys. Rev. Lett. **109**, (2012).

[21] A. Yan, J. Velasco Jr, S. Kahn, K. Watanabe, T. Taniguchi, F. Wang, M. F. Crommie, and A. Zettl, Nano Lett. **15**, 6324 (2015).

[22] See Suppl. Mater. (n.d.).

[23] W. Regan, N. Alem, B. Aleman, B. S. Geng, C. Girit, L. Maserati, F. Wang, M. Crommie, and A. Zettl, Appl. Phys. Lett. **96**, (2010).

[24] G. Kresse and D. Joubert, Phys. Rev. B **59**, 1758 (1999).

[25] G. Kresse and J. Furthmüller, Phys. Rev. B **54**, 11169 (1996).

[26] S. Grimme, J. Comput. Chem. **27**, 1787 (2006).

[27] J. A. Wilson and A. D. Yoffe, Adv. Phys. **18**, 193 (1969).

[28] G. Constantinescu, A. Kuc, and T. Heine, Phys. Rev. Lett. **111**, 36104 (n.d.).

[29] D. B. Williams and C. B. Carter, *The Transmission Electron Microscope* (Springer, 1996).

[30] E. J. Kirkland, *Advanced Computing in Electron Microscopy* (Springer Science & Business Media, 2010).

[31] W. Kohn and L. J. Sham, Phys. Rev. **140**, A1133 (1965).

[32] I. V Markov, *Crystal Growth for Beginners: Fundamentals of Nucleation, Crystal Growth, and Epitaxy*, 2nd ed. (World Scientific Publishing Company, 2003).